Journal of Nuclear Materials 409 (2011) 167–175

Contents lists available at ScienceDirect

Journal of Nuclear Materials

journal homepage: www.elsevier.com/locate/jnucmat

Further development of large-scale atomistic modelling techniques for Fe–Cr alloys

D. Terentyev [a,*], G. Bonny [a], N. Castin [a], C. Domain [b], L. Malerba [a], P. Olsson [b], V. Moloddtsov [c], R.C. Pasianot [d,e]

[a] SCK-CEN, Nuclear Materials Science Institute, Boeretang 200, B-2400 Mol, Belgium
[b] Dept. MMC, EDF-R&D, Site des Renardières, F-77218 Moret-sur-Loing, France
[c] SSCRF, The Institute of Physics and Power Engineering, 249020 Obninsk, Russia
[d] CAC-CNEA, Depto. de Materiales, Avda. Gral. Paz 1499, 1650 San Martín, Pcia. Buenos Aires, Argentina
[e] CONICET, Avda. Rivadavia 1917, 1033 Buenos Aires, Argentina

ARTICLE INFO

Article history:
Available online 16 October 2010

ABSTRACT

In this paper we review the current status of our efforts to model the Fe–Cr system, which is a model alloy for high-Cr ferritic–martensitic steels, using large-scale atomistic methods. The core of such methods are semi-empirical interatomic potentials. Here we discuss their performance with respect to the features that are important for an accurate description of radiation effects in Fe–Cr alloys. We describe their most recent improvements regarding macroscopic thermodynamic properties as well as microscopic point-defect properties. Furthermore we describe a new type of large-scale atomistic kinetic Monte Carlo (AKMC) approach driven by an artificial neural network (ANN) regression method to generate the local migration barrier for a defect accounting for the local chemistry around it. The results of the thermal annealing of the Fe–20Cr alloy modelled using this AKMC approach, parameterized by our newly developed potential, were found to be in very good agreement with experimental data. Furthermore the interaction of a 1/2 ⟨1 1 1⟩ screw dislocation with Cr precipitates as obtained from the AKMC simulations was studied using the same potential. In summary, we critically discuss our current achievements, findings and outline issues to be addressed in the near future development.

1. Introduction

The commonly proposed structural materials for advanced nuclear reactors such as fusion reactors, Gen IV fission reactors and accelerator driven systems are high-Cr ferritic–martensitic steels (~9–12 at.%Cr), possibly containing dispersed oxide particles (oxide-dispersion-strengthened, or ODS, steels). This choice is supported by their superior radiation resistance as compared to austenitic steels. Up to present, large international effort is devoted to extend the understanding of radiation damage effects in such steels by studying different phenomena in body centred cubic (bcc) model materials (e.g. [1,2]).

In recent years, the computer based multi-scale modelling approach has established itself as a promising tool for developing quantitative models to describe radiation effects in materials. Computer experiments can help interpret experimental data by separating the effects of the different physical processes causing the changes occurring in materials under irradiation and so reveal the fundamental physical mechanisms leading to a degradation of the material's properties. Computer models can also give access to phenomena that are impossible to observe experimentally, but are known to be at the origin of radiation damage (e.g. displacement cascades, properties of point-defects and their clusters, core effects on dislocations, etc.). However, these models cannot encompass the whole chemical complexity of real materials and appropriate reference model alloys must be selected for their application. A large number of experimental observations support the fact that chromium is the element that mainly determines the properties of ferritic martensitic high-Cr steels. We thus take the Fe–Cr binary model alloys as references for our modelling.

Amongst other irradiation induced and accelerated phenomena, binary Fe–*x*Cr alloys and high-Cr ferritic martensitic steels undergo α–α′ phase separation if the Cr content, x_{Cr}, exceeds ~9 at.% in the region of temperatures potentially important for technological applications (>600 K) [3–11]. The formation of finely-dispersed, nanometric-size Cr-rich precipitates (α′ phase) in the bulk (α phase) and at dislocations is long known to be the cause of hardening and embrittlement of high-Cr ferritic martensitic steels with $x_{Cr} > 14\%$ after thermal ageing (475 °C embrittlement [3–7]), as well as, at even lower temperature and Cr content, under irradiation, which is found to accelerate the phase separation process [9–11], or possibly induce it [12–14]. Therefore, a quantitative understanding of the kinetics of α–α′ decomposition and its impact on mechanical property changes in Fe–Cr alloys must be pursued.

In support of this endeavour, we present our latest developments regarding large-scale atomistic simulations in the Fe–Cr

* Corresponding author. Tel.: +32 14 333197; fax: +32 14 321216.
E-mail address: dterenty@sckcen.be (D. Terentyev).

0022-3115/$ - see front matter © 2010 Elsevier B.V. All rights reserved.
doi:10.1016/j.jnucmat.2010.09.024

binary. As a starting point, we present here our improved interatomic many-body potential for the Fe–Cr binary system (the full details on fitting methodology will be presented in [15]). This potential forms the core of the large-scale atomistic methods developed and applied as described in this paper. To simulate the microstructural evolution in the Fe–Cr alloys we present our recent developments regarding an innovative atomistic kinetic Monte Carlo (AKMC) technique [16]. The latter uses an artificial neural network (ANN) as a regression tool to predict the point-defect migration barrier for a given local chemical environment. In the case reported, the ANN is trained on a database of vacancy migration barriers consistently obtained with our interatomic potential. As a first validation of the ANN driven AKMC code, we simulate thermal annealing process in Fe–20at.%Cr at 773 K and compare the results, i.e. precipitate morphology, average size and density with available experiments done in a binary Fe–20 at.%Cr alloy. Subsequently, we use the AKMC results to study with the same interatomic potential, by molecular dynamics (MD) and static (MS) simulations, the interaction of a 1/2 ⟨1 1 1⟩ screw dislocation with Cr precipitates. We conclude the paper with a critical discussion on the limitations of the applied methods and present an outlook for our near future developments.

2. Background and methods

2.1. Role of Cr content in Fe–Cr alloys

The addition of chromium to iron influences significantly the response of the alloy to irradiation. It has been shown that the swelling in Fe–Cr is about one order of magnitude lower than in pure Fe at the same dose [12,17,18]. A remarkable effect of Cr is also observed in the shift of the ductile-to-brittle transition temperature (DBTT) in irradiated high-Cr ferritic–martensitic steels. This shift is found to reach a minimum around 9 at.%Cr [19], in a range of irradiation temperatures from 300 to 410 °C and for doses from 7 to 36 dpa. This result is in fact the main reason for the selection of Fe–9Cr as a basis for commercial reduced activation steels.

Even in the absence of irradiation, the Fe–Cr system exhibits a number of peculiarities. Density functional theory (DFT) calculations on the Fe–Cr binary have shown that the mixing enthalpy exhibits a change of sign [20–24], which is negative below a critical concentration ~10 at.%Cr and positive above it. A negative mixing enthalpy indicates full solubility and a tendency to partial ordering, while a positive value indicates that Cr atoms cluster into a separate Cr-rich phase (α′ phase). This is compatible with experimental results showing an inversion of the sign of the short-range order parameter from negative to positive, crossing zero at about 9–10 at.%Cr [25,26]. In turn, this behaviour is reflected in the Fe–Cr equilibrium phase diagram [27,28], which was recently revised [27,62] and consists of a meta-stable miscibility gap (when ignoring the sigma phase) with large Cr solubility even at low temperature (~8 at.%Cr below 750 K).

2.2. Interatomic potentials

In the literature two interatomic potentials have been developed in an embedded atom method (EAM)-like formalism capable of reproducing a complex behaviour of the mixing enthalpy as a function of composition. These potentials are (i) a two-band model (2BM) potential developed by Olsson et al. [29] (henceforth OLS) and (ii) a concentration dependent model (CDM) potential developed by Caro et al. [30] (henceforth CAR). The 2BM is a modification of the EAM, where a second embedding term is added to account for a contribution of *s*-band electrons. The CDM, on the other hand, keeps the EAM form but has a mixed pair interaction that depends on both distance and local concentration. Although formally different, both formalisms have been shown to be equally capable of reproducing the required mixing enthalpy shape of the Fe–Cr binary [31]. In addition, the OLS model (henceforth we refer to the potential fitted to DFT data obtained using the projector augmented wave approximation [29]) has proven to be an excellent potential with respect to the description of the interaction between Cr and point-defects in Fe (see [32,33] and references therein).

Both potentials, however, suffer from some important drawbacks. A first shortcoming concerns the pure elements, which in both cases are described by the same single-element potentials. In particular, the pure Fe potential developed by Ackland et al. [34] (henceforth A04) does not seem to provide stable glide of a 1/2 ⟨1 1 1⟩ screw dislocation in the {1 1 0} plane when subjected to a load [35], in contrast to experimental findings [36,37]. The pure Cr potential developed by Olsson et al. [29] (henceforth O05), on the other hand, does not predict a compact core of a 1/2 ⟨1 1 1⟩ screw dislocation, in contrast with direct DFT calculations [38] and atomic row method parameterized using DFT [39]. More regarding the limitations of both potentials applied to simulate dislocation movement can be found in Section 2.4.

Regarding the alloy, the OLS potential predicts stable intermetallic compounds at 50 at.%Cr and at the Cr-rich side (>90 at.%Cr), which are experimentally not observed and contradict to DFT calculations [40]. As a consequence of the latter, the mixing enthalpy is negative above 90 at.%Cr, again contrary to DFT calculations [20–24]. The CAR model, on the other hand, largely underestimates the experimentally observed excess vibrational entropy [40]. As a result, the phase diagram obtained with that potential fails to describe full solubility below melting temperature, while experimentally a full solubility is observed above 900 K. In addition, the interaction of Cr atoms with interstitial defects in a pure Fe matrix (i.e. dilute Fe–Cr alloys) is poorly described by the CAR potential, as are the vacancy migration barriers [33]. As described in what follows, our new Fe–Cr potential corrects most drawbacks and is therefore used in our AKMC and MD simulations to describe thermal ageing and dislocation-precipitate interaction in Fe–Cr binary alloys.

2.3. Atomistic kinetic Monte Carlo

In the framework of a rigid lattice AKMC method, the migration of point-defects (a single vacancy in our case) is driven by a local atomic environment (LAE)-dependent jump frequency $\Gamma = \upsilon_0 \times \exp(-E_m/k_B T)$. Here υ_0 is an attempt frequency (usually taken constant, for example, the Debye frequency of the host crystal), k_B is Boltzmann's constant, T is the absolute temperature and E_m is the LAE-dependent point-defect migration barrier. In this scheme, each defect jump corresponds to one MC step. The jump to be performed is chosen based on its probability, evaluated in terms of the corresponding jump frequency Γ. The time between two jumps is calculated according to the mean residence time algorithm, i.e. for a bcc lattice, by taking the inverse of the sum of the eight (only 1st nearest neighbour jumps are considered) possible jump frequencies. Thus, for a single MC step, E_m must be estimated eight times, if only one vacancy is present in the system. Accurate methods to estimate E_m, such as the drag method [41] or nudged elastic band (NEB) method [42] are time consuming and can not be effectively used in long-term AKMC simulations which typically cover $>10^5$ MC steps. Therefore a computationally efficient regression method capable of accurately reproducing the LAE-dependent vacancy migration barriers is necessary for any long-term large-scale AKMC simulations.

In the literature, heuristic methods are generally used to estimate the energy barriers. Broken bond methods are frequently used, see e.g. [43]. Other methods make use of the Kang–Weinberg

decomposition [44] to correlate the energy barrier with the total energy difference of the equilibrium state before and after the defect jump, considering the excess energy, that is used to define the barrier, as a constant. All of these methods, even when parameterized on *ab initio* reference data, lack accuracy to estimate the migration barriers for a variety of local chemical arrangements. In addition, these methods cannot account for lattice distortion effects, due for example to over- or under-sized solutes surrounding the migrating defect [45,46]. On the contrary, once trained the ANN regression scheme can predict local migration barriers with an accuracy of the same order as the NEB method, thereby fully accounting for chemical and relaxation effects (at 0 K), at a fraction of the computation time required by a full NEB calculation, i.e. with a speeding factor of 10^6.

Briefly, the ANN regression scheme takes as an input the LAE around the migrating defect and provides its migration barrier as output. The ANN regression scheme is trained once using an extended dataset of migration barriers for a defect (about 10^5 entries), calculated with the NEB method for a variety of LAEs. The generation of such a dataset is the time consuming step and can be obtained by applying interatomic potentials or *ab initio* techniques. Typically ~40% of the database is used to train the ANN, while ~60% is used to validate its predictive capability. A detailed description of the method and its successful application to vacancy diffusion in various alloys can be found in [16,46–48]. To conclude, we note that this method inherently includes 0 K relaxation effects which are thus indirectly taken into account in the AKMC approach we use, whereas the efficiency of a rigid lattice simulation is maintained.

2.4. Movement and interaction of a 1/2 ⟨1 1 1⟩ screw dislocation with precipitates in bcc Iron

In bcc metals and alloys there is a strong difference in Peierls stress between the screw and edge dislocations. The former has the Peierls stress which is about two orders of magnitude higher than the latter. Thus, the mobility of 1/2 ⟨1 1 1⟩ screw dislocations controls the slip and hence plasticity in bcc materials, at least below room temperature (see e.g. [49]). EAM potentials have been extensively used in the past to characterize properties of both edge and screw dislocations in bcc materials, in particular Fe (see [50] for a review). In general, EAM potentials were found to predict a degenerate symmetry-broken threefold core structure for a 1/2 ⟨1 1 1⟩ screw dislocation in bcc Fe [51,52] and Cr [50]. This result is, however, in contrast with data obtained using DFT, which suggests that all DFT-studied bcc metals of group VB and VIB exhibit an isotropic non-degenerate core structure [53–56]. A reliable prediction of the core structure is believed to be important for the adequate description of the Peierls barrier and a stable glide in a specific {1 1 0} plane. As discussed in [57], a 1/2 ⟨1 1 1⟩ screw dislocation can keep its original $(1\bar{1}0)$ glide plane if kink pairs are systematically nucleated in this plane, or if they nucleate in all three {1 1 0} planes of the [1 1 1] zone such that, on average, the dislocation glides on the (1 1 0) plane. The nucleation of kinks in the $(1\bar{1}0)$ plane in turn is only compatible with a non-degenerate core that retains the same configuration after each atomic move and can systematically emit kink pairs in the same plane. Recent refits of Ackland's potential for bcc Fe [34,58], have shown that the standard EAM formalism is good enough to reproduce a non-degenerate structure [59]. Nonetheless, as mentioned in Section 2.2, the potential from [58] predicts a stable glide of a 1/2 ⟨1 1 1⟩ screw dislocation in the (1 1 0) plane at finite temperature [57], while with the A04 potential the dislocation sometimes produces cross-slip events [35].

O05 Our potential for Cr, on the other hand, predicts a degenerate core structure [60]. Hence, one may expect that isotropic-to-degenerate core transformation may occur once the dislocation enters the precipitate. This was studied in [60] and it was shown that such a transformation indeed exists and yields in an additional increase of the interaction energy (i.e. increase of the repulsive interaction between the dislocation and precipitate). Since DFT data suggest a compact core structure for pure Cr [38,39], it is important to clarify the role of the core structure in the interaction mechanism. We thus perform comparative static and dynamic calculations using OLS and the newly refitted potential (which predicts isotropic core structure in pure Cr) to study the interaction of a 1/2 ⟨1 1 1⟩ screw dislocation with Cr precipitates in bcc Fe matrix.

3. Development of interatomic potential

In this section we compare the performance of the different potentials surveying the properties of direct interest to simulate thermal annealing and 1/2 ⟨1 1 1⟩ screw dislocation-precipitate interactions. For the former, a good reproduction of the experimental phase stability and local vacancy migration barriers are essential, while for the latter, a correct reproduction of the dislocation core structure and stable glide in a {1 1 0} plane are important. We mention, however, that our potential was fitted to many other properties that are summarized in Table 1, but not discussed in this paper (see [15] for a complete discussion). In this table we indicate how well properties calculated with the potentials compare to DFT and experimental data. We managed to develop a potential that corrects most of the important shortcomings mentioned in Sections 2.2.

The phase diagrams based on the three potentials (OLS, CAR and developed here) are plotted in Fig. 1. In all cases vibrational and configurational entropy were accounted for in a direct or indirect way (see [40,61] for details). In the same figure, a re-parameterization of the Calphad miscibility gap [62], based on [27,28] is added. When focussed on the Fe-rich side, we observe large Cr solubility at low temperature, due to the negative heat of mixing. As shown in the figure, this behaviour is well reproduced by all potentials. At about 750 K the Fe-rich solubility limit increases until full solubility is observed above ~900 K. The curve resulting from the OLS potential follows this trend at best, where full solubility is observed above ~1000 K, closely followed by the one from our potential. In the case of the CAR potential, on the other hand, no full solubility is observed below melting temperature. On the Cr-rich side, little Fe solubility is observed at low temperature, which is well reproduced by both our and the CAR potential. In contrast, the OLS potential predicts high Fe-solubility as an unphysical artefact of the negative heat of mixing at the Cr-rich side (see Section 2.2). Thus, from the viewpoint of phase stability, our potential seems the best choice.

In Fig. 2 we compare vacancy migration barriers for different LAEs calculated by the three potentials with DFT data [48]. The LAE configurations correspond to different Cr occupancies at first nearest neighbour positions around the migration saddle point in the bcc Fe matrix. This comparison shows that neither of the potentials provides a one-to-one agreement with the DFT values. However, the OLS and our potentials are clearly closer to the DFT data, especially for low migration energy values, i.e. relevant for the most frequent transitions. Globally, both our potential and OLS, with mean errors from the DFT values of 10% and 11%, respectively, perform better than the CAR potential, whose mean error is 23%. Based on the description of phase stability and vacancy migration barriers, our potential seems to be the most appropriate choice to simulate thermal annealing.

In Fig. 3, the differential displacement maps [63] for the 1/2 ⟨1 1 1⟩ screw dislocation core in Cr obtained using static relaxations with our potential and O05 potential are compared. The latter shows a threefold symmetry, while the core is compact according to the here developed potential, so, as predicted by

Table 1
Schematic summary of the performance of the different central-force interatomic potentials developed for Fe–Cr system.

Potential	Thermodynamics				Point-defects		
	Disordered alloy	Intermetallic compounds	Vibrational entropy	Substitutional	Interstitial	Vacancy	Dislocations
This work	Consistent	Consistent	Underestimated	Consistent	Consistent	Consistent	Consistent
OLS	Inconsistent	Inconsistent	Overestimated	Consistent	Consistent	Consistent	Inconsistent
CDM	Consistent	Consistent	Inconsistent	Consistent	Inconsistent	Inconsistent	Inconsistent

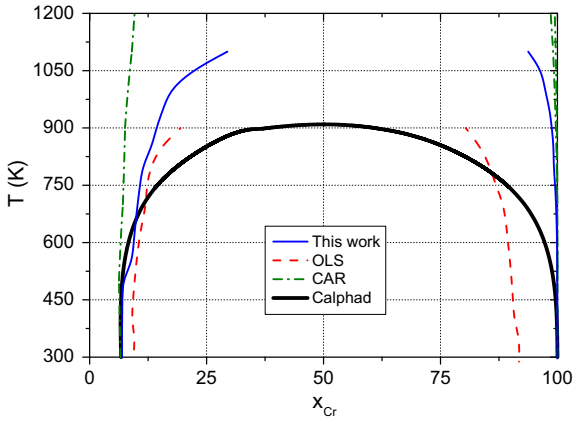

Fig. 1. Comparison of the phase diagrams resulting from the different potentials with the Calphad data. The curves for the OLS, CAR and Calphad models were taken from [40,62,63,27], respectively.

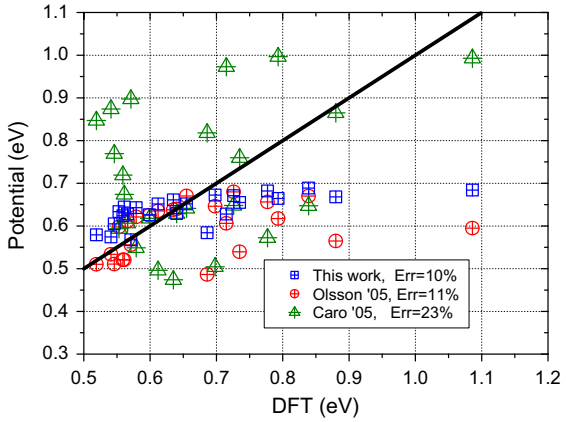

Fig. 2. Comparison of vacancy migration barriers in the Fe-matrix for different local Cr configurations between the different potentials and DFT [48].

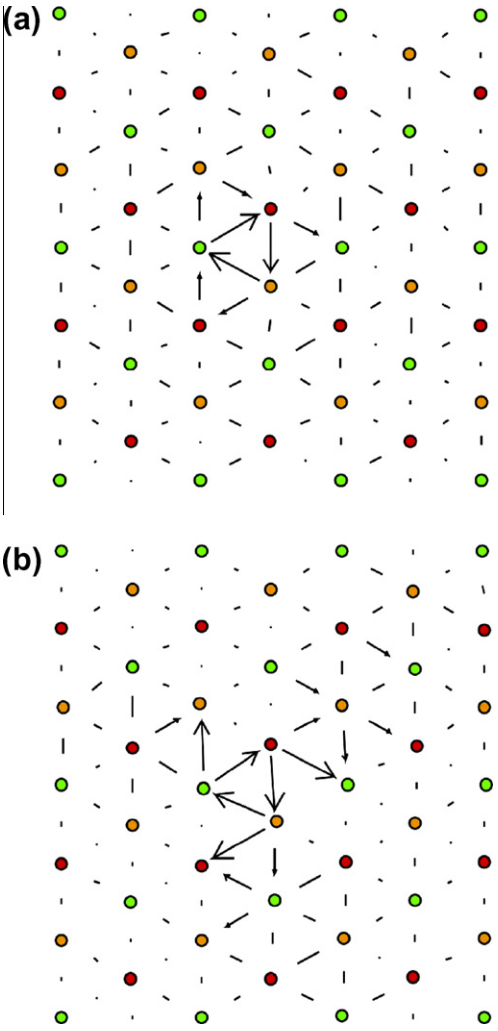

Fig. 3. Core of a 1/2 ⟨1 1 1⟩ screw dislocation obtained using our newly developed potential (a) and O05 potential (b). The ⟨1 1 1⟩ direction is normal to the paper, atoms are shown in ⟨1 1 1⟩ projection distributed in three different layers (indicated by the circles with different contrast) separated by the distance a/6 ⟨1 1 1⟩. The screw component of differential displacement is depicted as an arrow, with length proportional to the magnitude of displacement, positioned between relevant pair of atoms.

DFT [38]. As mentioned in Section 2.4, a correct reproduction of the dislocation core structure is *a priori* important to obtaine adequate results from dynamic simulations. Recalling that the potential from Ref. [58] provides a stable glide in a (1 1 0) and A04 not necessarily (see Sections 2.2 and 2.4), we believe that our newly fitted Fe–Cr potential suits better to simulate the interaction of a 1/2 ⟨1 1 1⟩ screw dislocation with Cr precipitates.

4. Development of atomistic kinetic Monte Carlo

Prior to presenting the results of our simulations of thermal annealing, we discuss the reliability of the ANN regression scheme obtained. In Fig. 4 the barriers calculated with NEB using our potential are compared to the ANN predicted values. With an average error of 3.8% and correlation factor of 0.99, we can conclude that using the ANN to estimate the vacancy migration energy in the AKMC cycle is equivalent to doing NEB calculations on the fly. To give an idea about the performance of heuristic methods such as the Kang–Weinberg decomposition [44], we show the data obtained with the newly developed potential. The average error was estimated to be 27% and the correlation factor is less then 0.1. Therefore we believe that, at present, the ANN regression provides the best compromise between accuracy and computational speed, at least in the case of vacancy migration in concentrated Fe–Cr alloys.

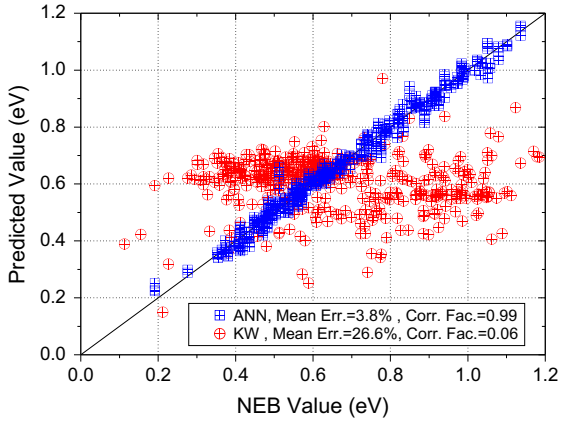

Fig. 4. Comparison of the LAE-dependent vacancy migration barriers, being estimated with the NEB, ANN and KW-type methods.

The thermal annealing of an Fe–20%Cr alloy at 773 K was simulated in a cubic box containing 0.128 M atoms with an initial random distribution of Cr atoms. The evolution of the system leading to the atomic redistribution was driven by a single vacancy. The thermal annealing process was simulated until the coarsening regime was reached, for the reasons discussed below. During the AKMC simulation, the formed precipitates were characterized in terms of average size and density, using a numerical treatment presented in [64,33]. For an adequate comparison of the obtained size and density evolution with experiments, AKMC time (t_{MC}) was renormalized to account for the discrepancy in the vacancy concentration in the modelled crystal ($C_V^{MC} = 1/128{,}000$) and in the real specimen during annealing (C_V^{real}) [65]. Following Refs. [66,33] we rescaled the t_{MC} so as to fit the first experimental data point for the average precipitate size.

The average precipitate diameter and density are presented in Fig. 5 as a function of annealing time, together with experimental data obtained by small angle neutron spectroscopy (SANS) [8] and atom probe (AP) [67]. From our simulations, we could identify the different stages of the precipitation process, namely, nucleation, growth and coarsening.

Reasonably good quantitative agreement with experiments is obtained for both presented curves, given that only the average precipitate diameter was fitted using the first data point from Ref. [8]. It thus seems that our potential in combination with the ANN driven AKMC technique forms an excellent tool to study the early stages of α–α′ phase separation under thermal annealing conditions. The last stage, i.e. the coarsening process proceeds very slowly and can not be efficiently studied with the present tools, as discussed in Section 6.

5. Modelling of dislocation – precipitate interaction

In this section we describe the results of atomistic simulations performed to study the mechanisms of interaction of a 1/2 ⟨1 1 1⟩ screw dislocation with Cr precipitates in the bcc Fe matrix. Although in the case of α–α′ phase separation Cr precipitates are present in a concentrated solid-solution, we consider a pure Fe matrix and Cr precipitates extracted from the AKMC simulations (see Section 4), because these simulations provide exclusive information about effects related to the Cr precipitate alone, avoiding possible background 'noise' due to Cr in solid-solution. Even though the latter can be important, their statistical treatment is time consuming and not straightforward. The comparative study using both two-band model potentials (OLS and ours) is divided into two parts. Firstly, we perform static simulations to investigate the

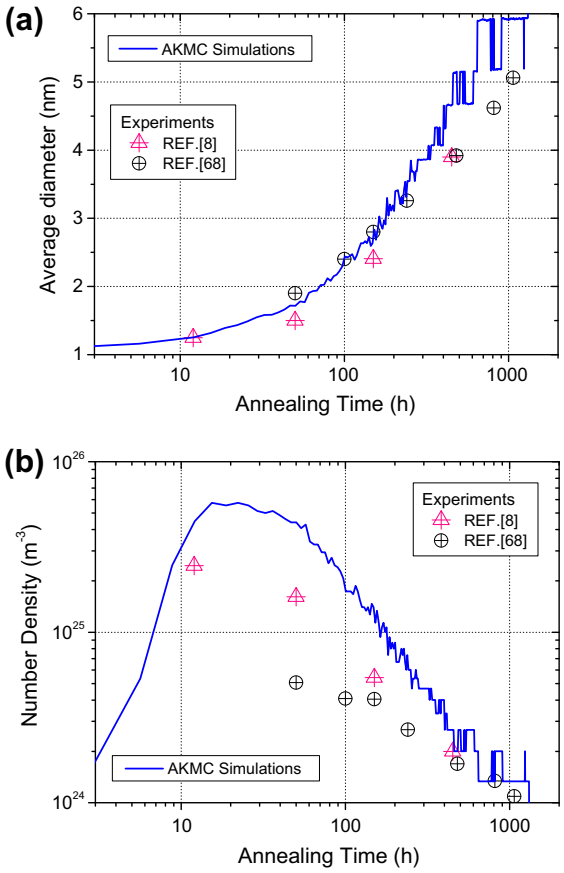

Fig. 5. (a) Average precipitate size and (b) density versus experimental annealing time and compared with experimental data [8,67].

effects of Cr precipitates on the dislocation core structure and estimate the interaction energy between the dislocation and precipitate as a function of distance and precipitate size. In these simulations we considered precipitates with diameters ranging from 1 to 5 nm, following the results obtained from the AKMC simulations (see Section 4). Secondly, we performed dynamic simulations to model the interaction of the dislocation with a 2 nm Cr precipitate at $T = 300$ and 600 K. The interaction mechanism and related stress–strain curves are then analyzed and compared.

5.1. Static simulations

For our simulations we used a bcc simulation box of $20 \times 12 \times 28\ \text{nm}^3$ with principal axes oriented along the $[\bar{1}\,\bar{1}\,2]$, $[1\,\bar{1}\,0]$ and $[1\,1\,1]$ directions. Periodic boundary conditions were only applied in the $[1\,1\,1]$ direction and following [59] a straight screw dislocation with left-handed thread and Burgers vector $b = 1/2\ [1\,1\,1]$ was created in this direction, as schematically shown in Fig. 6. Following this, a Cr precipitate was inserted at a defined distance from the dislocation line with centre in the $(1\,\bar{1}\,0)$ glide plane. Several such configurations were then relaxed for different precipitate-dislocation distances and precipitate sizes (diameter 2, 3, 4 and 5 nm) and their interaction energy E_I was estimated (positive values indicating repulsive interaction). For more details the reader is referred to similar calculations performed in [52,60].

The results of these calculations are presented in Fig. 7 for the OLS (figure a) and our potential (figure b), respectively. From the figure we observe that the dislocation interacts repulsively with the precipitate, as is expressed by the increase of the interaction

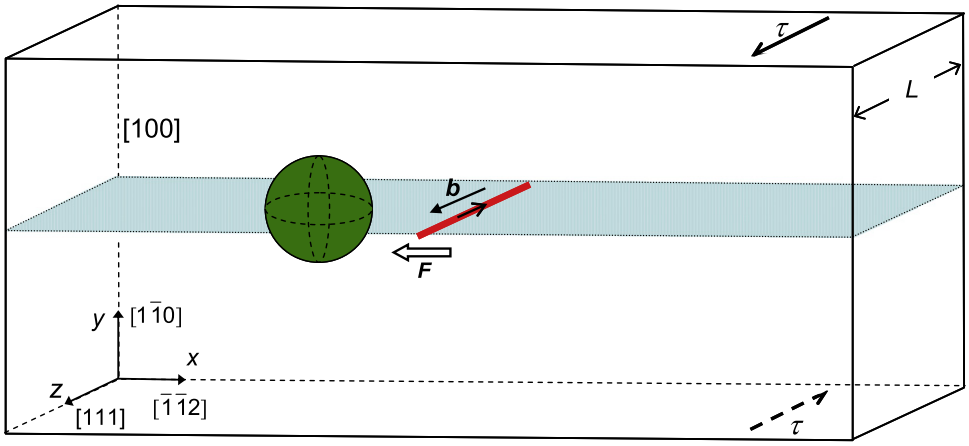

Fig. 6. Geometry of the interactions considered. The sketch illustrates the position of the precipitate before interaction with the left-handed screw dislocation line. The glide plane of the screw dislocation is $(1\,\bar{1}\,0)$ and it moves in the $[1\,1\,\bar{2}]$ direction under the applied shear stress τ.

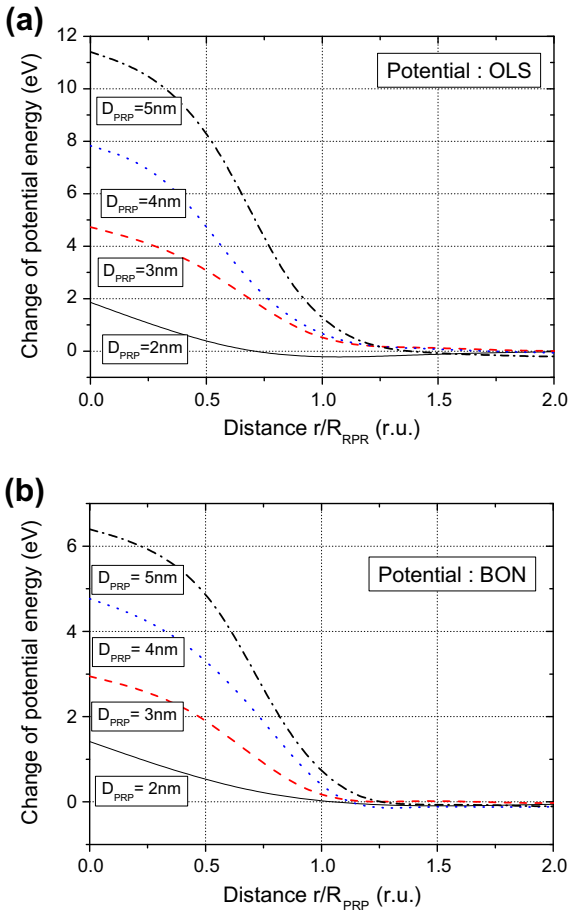

Fig. 7. Interaction energy of the screw dislocation (moving in the $(1\,\bar{1}\,0)$ plane in the $[\bar{1}\,\bar{1}\,2]$ direction) with Cr precipitates of different sizes estimated using static simulations. Interaction geometry is shown in Fig. 6.

energy that reaches a maximum in the precipitate centre. For the OLS potential the maximum of E_I is, however, about twice as high as for our potential. Another important observation, seen with both potentials, is that the largest gradient of E_I (i.e. the maximum force) occurs at ~70% of the precipitate radius. Note that for the OLS potential this value is consistently 30–40% higher than for our potential. An in-depth analysis of the interaction energy and contributions originating from different sources (chemical energy, shear modulus misfit, core energy misfit) is given in [60]. Here we only mention that the contribution from the modulus misfit was found to be the highest among the others in the case of the OLS potential. In the same work it was also shown that the core energy misfit, which can be explicitly accounted for with the aid of atomistic simulations in the shear modulus misfit model, is not negligible. This in turn shows the importance of the compact-to-degenerate core transformation at the moment when the dislocation enters the Cr precipitate. In the simulations with our potential, no such transformation was observed. At the same time, the shear moduli estimated by shearing ($\langle 1\,1\,1\rangle\{1\,1\,0\}$ loading mode) pure Cr crystals, were calculated to be 130 and 89 GPa for the OLS and our potential. The combined effects explain the higher values for E_I obtained with the OLS potential.

To summarize, according to our static results, the maximum force needed to shear a Cr precipitate at its centre is about 40% smaller with our potential than according to the OLS model. In what follows we present the results of dynamic simulations.

5.2. Dynamic simulations

For dynamic simulations, the model crystal was divided along the [1 1 1] direction into three blocks of atoms. Those in the central region were free to move in the MD cycle, whereas those in the upper and lower blocks were held rigidly in their original position with respect to their neighbours in the same block. The size of the inner region was $21 \times 7.5 \times 20\ \text{nm}^3$. External action to induce the dislocation to glide was applied by simultaneous displacement of the upper and lower blocks in the [1 1 1] direction to produce the shear strain e_{xz}. This procedure results in a force per unit length $F = \tau b$ in the $[1\,1\,\bar{2}]$ direction for glide of the left-handed screw dislocation on the $(1\,\bar{1}\,0)$ plane (see Fig. 6). The induced shear stress τ was calculated from the external force exerted on the blocks by the atoms in the central region. Strain was applied at a constant rate $\dot{\varepsilon} = 3.43 \times 10^7\ \text{s}^{-1}$ to boxes previously equilibrated at the temperature, $T = 300$ or 600 K. The steady state velocity, v_D, of an isolated dislocation at this strain rate was estimated from the Orowan relation (e.g. [68]) $\dot{\varepsilon} = \rho_D b v_D$ between strain rate and dislocation density ρ_D ($=6.5 \times 10^{15}\ \text{m}^{-2}$) to be 21 ms^{-1}. To visualize the interaction mechanisms in detail, we have identified the dislocation core using an analysis described in [69]. From our simulations we observed that the motion of the dislocation proceeds via the nucleation of kink pairs and their propagation along the dislocation line. In MD simulations, in the specified range of temperature and strain rate here applied, the velocity of the dislocation is controlled

by the rate of nucleation of stable kink pairs, which is a probabilistic event. Hence, a typical stress–strain curve, such as the one shown in Fig. 8a, consists of a set of irregular saw-like peaks, whose height and interspacing fluctuate. To see the relation between the stress state and dislocation movement we displayed its evolution in a (1 1 1) plane. The evolution along the $[\bar{1}\,\bar{1}\,2]$ direction gives information about advance of the dislocation core in the $(1\,\bar{1}\,0)$ glide plane, while the evolution along the $[1\,\bar{1}\,0]$ direction determines the cross-slip movement. Such a typical loading diagram is also shown in Fig. 8a for the dislocation moving in pure Fe at 300 K.

The loading diagrams shown in Fig. 8b and c correspond to a dislocation interacting with a 2 nm precipitate at $T = 300$ K, simulated using both the OLS and our potentials, respectively. The interaction process is described as follows. The dislocation moves towards the precipitate under constantly increasing stress. As soon as the dislocation reaches the precipitate matrix interface it starts to curve around the precipitate. This behaviour was observed with both potentials. From this point onwards, however, the interaction mechanism differs. In the simulations with the OLS potential, the dislocation cross slips downwards in the inclined {1 1 0} plane across the precipitate surface, as can be seen from the core evolution along the $[1\,\bar{1}\,0]$ direction in Fig. 8b. The dislocation line moves under the precipitate and gets pinned at its bottom. When the resolved stress reaches 550 MPa, the dislocation cross-slips up (again over the precipitate surface) and detaches, leaving the precipitate unsheared. The cross-slip events were clearly seen to be related with the emission of kink pairs at the precipitate matrix interface where the compact-to-degenerate core transformation takes place.

In simulations with our potential, the dislocation enters the precipitate at a stress of about 360 MPa and after a few successive jumps gets blocked again inside the precipitate. This occurs due to the excess of the friction stress for the screw dislocation inside the Cr precipitate. Indeed, the difference in the Peierls stresses in Fe and Cr computed from static simulations, is ~550 MPa for both potentials. After applying a substantial load (of 1.2%) resulting in the resolved shear stress equal to 370 MPa, the dislocation leaves the sheared precipitate. As can be seen from Fig. 8c, two single cross-slip events occurred during the interaction process while the dislocation was shearing the precipitate. Firstly the dislocation core was shifted up and then moved down, back to the original glide plane. Similar difference in the interaction mechanisms modelled with both potentials was found in simulations at 600 K.

As was shown, the interaction mechanisms seen in dynamic simulations differ significantly for the two potentials. Both potentials predict similar difference for the Peierls stress of a 1/2 ⟨1 1 1⟩ screw dislocation in Fe and Cr, but different core structures. It therefore seems that the latter feature determines the cross-slip around the precipitate, observed with the OLS potential. From the view point of the dislocation core structure, the results obtained with our potential are considered to be more realistic. However, a sensitivity of the two observed mechanisms to ambient temperature, precipitate size, dislocation length and applied strain rate is still to be studied, as well as features of the potential that govern the cross-slip of the dislocation around the precipitate. This will be addressed in our future work.

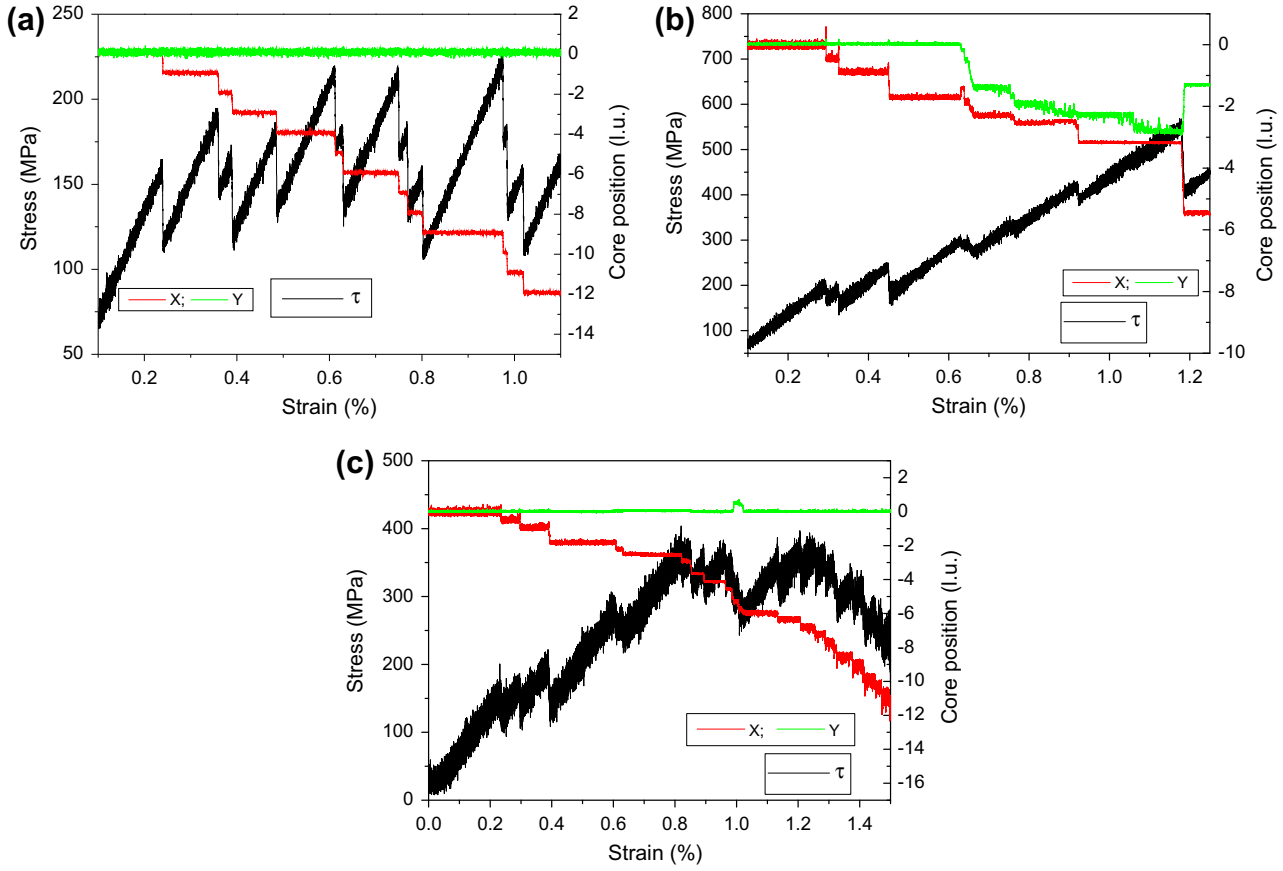

Fig. 8. Stress–strain loading diagrams: (a) screw dislocation in pure Fe and $T = 300$ K, modelled using the OLS potential; (b) screw dislocation interacting with a 2 nm precipitate at $T = 600$ K, modelled using the OLS potential; (c) screw dislocation interacting with a 2 nm precipitate at $T = 600$ K, modelled using the newly developed potential. The evolution of position of the dislocation core on the [1 1 1] plane is also shown.

6. Concluding remarks and summary

Prior to summarizing the presented results and drawing conclusions, we critically discuss our achievements and outline our current and near future developments. The first and probably most essential point of this discussion is the application of central force type many-body potentials to describe ferromagnetic metals and alloys. Clearly, such a formalism cannot describe magnetic interactions and their response to temperature, especially related to magnetic entropy, for example the ferromagnetic-to-paramagnetic transformation in pure iron at the Curie temperature. However, central force type potentials can satisfactorily describe DFT data at 0 K in the ferromagnetic phase and can account correctly for vibrational entropy effects at finite temperature. The reliability of central force type potentials applied to describe defect properties of the complex Fe–Cr system has proven to be reasonably accurate, as shown in [32,70]. The application of more involved formalisms, such as spin lattice dynamics [71], to correctly account for magnetic interactions is highly desirable, but has not yet reached sufficient level of maturity for routine and widespread use, such as for classical molecular dynamics. It must be noted, in addition, that advanced techniques come at the price of computational efficiency and therefore more approximate methods as central force type potentials remain useful for large-scale atomistic simulations.

The ANN regression method applied here was trained to predict vacancy migration energies, thereby relying on the trustworthiness of our potential. Since the ANN regression performs with an accuracy comparable to the NEB method itself, the limiting factor is the accuracy of the potential. The issue of training the ANN using directly a DFT dataset is the limited number of configurations that can be obtained in a reasonable amount of time. Experience gained using central-force interatomic potentials shows that the optimal regression is obtained for vast databases, containing about 10^5 configurations. Currently efforts are taken to prepare an extended DFT dataset for vacancy migration barriers, and at the same time to optimise the ANN regression training, so as to use as small database as possible.

Another disadvantage of any rigid lattice Monte Carlo technique is the natural absence of any possible structural transformation and the ignorance of the vibrational entropy (besides the magnetic one, due to the limitations of the potential formalism). Considering the problem of α–α' phase separation in Fe–Cr alloys (with content less than 20%Cr), however, the formation of non-coherent phases can be excluded. The vibrational entropy, on the other hand, may play important role in finding the equilibrium state. Nonetheless, for the kinetic problem, the vibrational entropy term is of the second priority, as it only modifies the prefactor in the attempt frequency and is less sensitive to changes of temperature than the exponential part of the expression for the jump frequency.

In the simulated thermal annealing experiment we have only accounted for mass transport by vacancy diffusion, as the vacancy concentration is several orders of magnitudes larger than interstitial concentrations under these conditions. Under irradiation, however, mass transport assisted by interstitials can become important, and may even lead to non-equilibrium precipitation on sinks. Currently, we are developing an ANN regression scheme and AKMC technique to account for both vacancy and interstitial diffusion to be able to describe the microstructural evolution of Fe–Cr under irradiation conditions.

Finally, even though our ANN driven AKMC code essentially improves accuracy without loss of computational speed, the problem of time and length scale for the coarsening process remains unsolved. Indeed, statistically reliable modelling of coarsening, which is characterized by large precipitates and low densities, requires the usage of extremely large simulation crystals and therefore narrows possible simulation time. So far, no fully established solution to this problem exists, except resorting to parallelisation techniques [72] which, however, have not yet been applied to treat complex problems.

To summarize, we have applied and combined different atomic-scale simulation techniques to study α–α' phase separation in the Fe–20Cr alloy. Firstly, we presented our newly developed Fe–Cr potential. Compared to existing ones, the potential we developed is improved with respect to a correct description of the core structure of a 1/2 ⟨1 1 1⟩ screw dislocation in Cr, a good description of the vacancy migration barriers and a phase diagram in a good agreement with the experimental one, obtained for ferromagnetic Fe–Cr alloys. The developed potential was applied to model thermal annealing of Fe–20Cr using the ANN driven AKMC technique. The obtained time evolution for average precipitate size and density was found to be in a good agreement with experiments. The precipitate configurations obtained were subsequently used to study the interaction of a 1/2 ⟨1 1 1⟩ screw dislocation with Cr precipitates using both originally and improved two-band model potentials. Preliminary results, whose thorough analysis will follow, already revealed an essential difference in the interaction energy and mechanisms between the two potentials. In the case of the OLS potential, the dislocation was found to cross-slip under a 2 nm precipitate, thus avoiding its shearing. In simulations with our new potential the dislocation kept gliding in a {1 1 0} plane and sheared the precipitate.

Acknowledgements

This research was supported by the EURATOM 7th Framework Programme, under Grant Agreement No. 212175 (GetMat Project) and by the European Fusion Development Agreement (Mat-Remev task). RCP acknowledges support from CONICET-PICT 5062. Part of the calculations was performed at the supercomputer facilities JUROPA within the APM project.

References

[1] (a) M. Victoria, S.L. Dudarev, J.L. Boutard, E. Diegele, et al., Fusion Eng. Des. 82 (2007) 2413;
(b) L. Malerba, A. Caro, J. Wallenius, J. Nucl. Mater. 382 (2008) 112.
[2] S.L. Dudarev, J.-L. Boutard, R. Laesser, M.J. Caturla, P.M. Derlet, M. Fivel, et al., J. Nucl. Mater. 386 (2009) 1.
[3] R.M. Fisher, E.J. Dulis, K.G. Carroll, Trans. AIME 197 (1953) 690.
[4] R.O. Williams, H.W. Paxton, J. Iron Steel Inst. 185 (1957) 358.
[5] R. Lagneborg, Trans. ASM 60 (1967) 67.
[6] P.J. Grobner, Metall. Trans. 4 (1973) 251.
[7] P. Jacobsson, Y. Bergström, B. Aronsson, Metall. Trans. 6A (1977) 1577.
[8] F. Bley, Acta Metall. Mater. 40 (1992) 1505.
[9] P. Dubuisson, D. Gilbon, J.L. Séran, J. Nucl. Mater. 205 (1993) 178.
[10] M.H. Mathon, Y. De Carlan, G. Geoffroy, X. Averty, C.H. de Novion, A. Alamo, in: S.T. Rosinski, M.L. Grossbeck, T.R. Allen, A.S. Kumar (Eds.), Effects of Radiation on Materials: 20th International Symposium, ASTM STP 1405, American Society for Testing and Materials, West Conshohocken, PA 674, 2001.
[11] M.H. Mathon, Y. de Carlan, G. Geoffroy, X. Averty, A. Alamo, C.H. de Novion, J. Nucl. Mater. 312 (2003) 236.
[12] E.A. Little, D.A. Stow, J. Nucl. Mater. 87 (1979) 25.
[13] E. Wakai, A. Ishinuma, Y. Kato, H. Yano, S. Takaki, K. Abiko, J. Physique IV, C7, Suppl. J. Physique III, 5 (1995) C7-277.
[14] E. Wakai, A. Hishinuma, K. Usami, Y. Kato, S. Takaki, K. Abiko, Mater. Trans. Jpn. Inst. Metal. 41 (2000) 1180.
[15] G. Bonny, R. Pasianot, in preparation (for methodology see Ref. [31]).
[16] N. Castin, L. Malerba, J. Chem. Phys. 132 (2010) 074507.
[17] E.A. Little, R. Bullough, M. Wood, Proc. Royal Soc. Lond A 372 (1980) 565.
[18] F.A. Garner, M.B. Toloczko, B.H. Sencer, J. Nucl. Mater. 276 (2000) 123.
[19] A. Kohyama, H. Matsui, K. Abe, K. Hamada, K. Asano, J. Nucl. Mater. 155–157 (1988) 1354.
[20] P. Olsson, I.A. Abrikosov, L. Vitos, J. Wallenius, J. Nucl. Mater. 321 (2003) 84.
[21] A.A. Mirzoev, M.M. Yalalov, D.A. Mirzaev, Phys. Metal Metall. 97 (2004) 336.
[22] T.P.C. Klaver, R. Drautz, M.W. Finnis, Phys. Rev. B 74 (2006) 094435.
[23] M.Yu. Lavrentiev, R. Drautz, D. Nguyen-Manh, T.P.C. Klaver, S.L. Dudarev, Phys. Rev. B 75 (2007) 14208.
[24] P. Olsson, C. Domain, J. Wallenius, Phys. Rev. B 75 (2007) 014110.
[25] I. Mirabeau, M. Henion, G. Parette, Phys. Rev. Lett. 53 (1984) 687.
[26] N.P. Filippova, V.A. Shabashov, A.L. Nikolaev, Phys. Metal Metall. 90 (2000) 145.

[27] G. Bonny, D. Terentyev, L. Malerba, Scripta Mater. 59 (2008) 1193.
[28] J.-O. Andersson, B. Sundman, CALPHAD 11 (1987) 83.
[29] P. Olsson, J. Wallenius, C. Domain, K. Nordlund, L. Malerba, Phys. Rev. B 72 (2005) 214119.
[30] A. Caro, D.A. Crowson, M. Caro, Phys. Rev. Lett. 95 (2005) 75702.
[31] G. Bonny, R.C. Pasianot, L. Malerba, Philos. Mag. 89 (2009) 711.
[32] D. Terentyev, P. Olsson, T.C.P. Klaver, L. Malerba, Comput. Mater. Sci. 43 (2008) 1183.
[33] G. Bonny, D. Terentyev, L. Malerba, Phys. Rev. B 79 (2009) 104207.
[34] G.J. Ackland, M.I. Mendelev, D.J. Srolovitz, et al., J. Phys.: Condens. Matter 16 (2004) S2629.
[35] F. Willaime, private communication (2009).
[36] F. Louchet, L.P. Kubin, Acta Metall. 23 (1975) 17.
[37] H. Matsui, K. Kimura, Mater. Sci. Eng. 24 (1976) 247.
[38] C. Domain, private communication (2010).
[39] Z. Chen, N. Kioussis, N. Ghoniem, T. Hasebe, Phys. Rev. B 77 (2008) 014103.
[40] G. Bonny, R.C. Pasianot, L. Malerba, A. Caro, P. Olsson, M.Yu. Lavrentiev, J. Nucl. Mater. 385 (2009) 268.
[41] G. Henkelman, G. Johannensson, Progress on Theoretical Chemistry and Physics, in: S.D. Swartz (Ed.), Kluwer Academic Publishers, 2000 269–300.
[42] G. Henkelman, H. Jonsson, J. Chem. Phys. 113 (2000) 9978.
[43] Y. Le Bouar, F. Soisson, Phys. Rev. B 65 (2002) 094103.
[44] H.C. Kang, W.H. Weinberg, J. Chem. Phys. 90 (1989) 2824.
[45] F.G. Djurabekova, R. Domingos, G. Cerchiara, N. Castin, E. Vincent, L. Malerba, Nucl. Instr. Meth. B 255 (2007) 8.
[46] N. Castin, L. Malerba, Nucl. Instrum. Meth. Phys. Res. B 267 (2009) 3148.
[47] N. Castin, R.P. Domingos, L. Malerba, Intl. J. Comp. Intell. Sys. 1 (2008) 340.
[48] N. Castin, G. Bonny, D. Terentyev, M.Yu. Lavrentiev, D. Nguyen-Manh, J. Nucl. Mater. in press.
[49] L.P. Kubin, Rev. Deformation Behav. Mater. 1 (1976) 243.
[50] M.S. Duesbury, V. Vitek, Acta Mater. 46 (1998) 1481.
[51] A.H.W. Ngan, M. Wen, Comput. Mater. Sci. 23 (2002) 139.
[52] T. Harry, D.J. Bacon, Acta Mater. 50 (2002) 209.
[53] S. Ismail-Beigi, T.A. Arias, Phys. Rev. Lett. 84 (2000) 1499.
[54] L. Ventelon, F. Willaime, J. Computer-Aided Mater. Des. 14 (2007) 85.
[55] S.L. Frederiksen, K.W. Jacobsen, Philos. Mag. 83 (2003) 365.
[56] F. Shimizu, S. Ogata, T. Kano, J. Li, F. Kaburaki, J. Earth Simulator 7 (2007) 17.
[57] J. Chaussidon, M. Fivel, D. Rodney, Acta Mater. 54 (2006) 3407.
[58] M.I. Mendelev, S.W. Han, D.J. Srolovitz, G.J. Ackland, D.Y. Sun, M. Asta, Philos. Mag. A 83 (2003) 3977.
[59] C. Domain, G. Monnet, Phys. Rev. Lett. 95 (2005) 215506.
[60] D. Terentyev, G. Bonny, L. Malerba, Nucl. Instr. Meth. Phys. Res. B 267 (2009) 3155.
[61] G. Bonny, P. Erhart, A. Caro, R.C. Pasianot, L. Malerba, M. Caro, Model. Simul. Mater. Sci. Eng. 17 (2009) 025006.
[62] G. Bonny, D. Terentyev, L. Malerba, J. Phase Equilib. Diff. 31 (2010) 439.
[63] V. Vitek, R.C. Perin, D.K. Bowen, Phil. Mag. 21 (1970) 1049.
[64] G. Bonny, D. Terentyev, L. Malerba, Comput. Mater. Sci. 42 (2008) 107.
[65] J.W. Martin, Micromechanisms in Particle-Hardened Alloys, Cambridge University Press, Cambridge, England, 1980.
[66] E. Vincent, C.S. Becquart, C. Pareige, P. Pareige, C. Domain, J. Nucl. Mater. 373 (2008) 387.
[67] S. Novy, P. Pareige, C. Pareige, J. Nucl. Mater. 384 (2009) 96.
[68] D. Hull, D.J. Bacon, Introduction to Dislocations, 4th ed., Butterworth-Heinemann, Oxford, 2001.
[69] D. Terentyev, P. Grammatikopoulos, D.J. Bacon, Yu.N. Osetsky, Acta Mater. 56 (2008) 5034.
[70] D. Terentyev, N. Castin, Comput. Mater. Sci. 46 (2009) 1178.
[71] Pui-Wai Ma, C.H. Woo, S.L. Dudarev, Phys. Rev. B 78 (2008) 024434.
[72] E. Martinez, J. Marian, M.H. Kalos, J.M. Perlado, J. Comput. Phys. 227 (2008) 3804–3823.